*International Journal of Minerals, Metallurgy and Materials*
*Volume 30, Number 4, April 2023, Page 724*
**https://doi.org/10.1007/s12613-022-2434-3**

# Microstructure and toughness of thick-gauge pipeline steel joint via double-sided friction stir welding combined with preheating

*Guangming Xie*✉, *Ruihai Duan*, *Yuqian Wang*, *Zong'an Luo*, *and Guodong Wang*

State Key Laboratory of Rolling and Automation, Northeastern University, Shenyang 110819, China
(Received: 2 December 2021; revised: 30 January 2022; accepted: 7 February 2022)

**Abstract:** Fusion welding easily causes microstructural coarsening in the heat-affected zone (HAZ) of a thick-gauge pipeline steel joint. This is most significant in the inter-critically coarse-grained HAZ (ICCGHAZ), which considerably deteriorates the toughness of the joint. In the present work, 11-mm thick pipeline steel was joined by preheating and double-sided friction stir welding (FSW). A comparative study on the microstructure and toughness in the ICCGHAZs for FSW and gas metal arc welding (GMAW) was performed. The toughness in the ICCGHAZ for FSW was improved significantly than that in the ICCGHAZ for GMAW. Generally, the nugget zone (NZ) has a coarse microstructure in the FSW steel joint formed at the highest peak temperature. However, in the current study, the microstructure in the one-pass NZ was remarkably refined owing to the static recrystallization of ferrite. An excellent toughness was achieved in the NZ of the pipeline steel joint that employed FSW.

**Keywords:** pipeline steel; thick-gauge plate; friction stir welding; microstructure; toughness

## 1. Introduction

Thick-gauge pipeline steel (thickness ≥ 10 mm) is widely utilized in oil and gas transportation [1–3]. Therefore, the welding process forms an essential procedure to ascertain the supply of quality products. For example, multi-pass welding is often required to join thick-gauge pipeline steel plates. However, multi-heating can generate an inter-critically coarse-grained heat-affected zone (ICCGHAZ) containing coarse network-like martensite–austenite (M–A) constituents, which can significantly deteriorate the toughness of the joint [4–6]. Therefore, controlling ICCGHAZ is necessary for obtaining a high-quality joint.

Friction stir welding (FSW) is a low-heat input joining technique owing to its solid-state nature [7]. In the FSW process, the low-heat input and fast post-welding cooling rate of the treated pipeline steel effectively inhibit the coarsening of both the grains and M–A constituents, thereby improving the toughness of the joint [8–9]. Currently, FSW is mainly used to join the thin-gauge pipeline steel (≤6 mm thickness), but the study on FSW thick-gauge pipeline steel is few [10–12]. This is attributed to the root defects easily appearing in the thick-gauge pipeline steel joint owing to insufficient plastic flow [13]. Besides, the thick-gauge steel with high deformation resistance may cause significant wear or destruction of the welding tool at elevated temperatures during FSW process [14]. Recently, some researchers tried to utilize double-sided FSW to join the thick-gauge pipeline steel and indicated that no obvious root defects and tool wear are observed [15–17]. Aydin and Nelson [15] conducted double-sided FSW in 11-mm-thick pipeline steel and obtained a joint without any defect. However, the toughness of the joint was not investigated. In addition, Avila *et al.* [16] evaluated the toughness in the nugget zone (NZ) and heat-affected zone (HAZ) of 15-mm-thick pipeline steel joint by double-sided FSW and detected the joint contains some various subzones. Obviously, for the double-sided FSW joint, according to various thermal cycle histories and welding passes, the HAZ and NZ can be divided into many subzones, which creates a complex effect on the microstructure and toughness. To date, few studies on the subzones of double-sided FSW steel joints have been reported.

In this study, 11-mm-thick high-strength bainitic pipeline steel was joined by a double-sided FSW process. Preheating of the steel before welding was carried out to reduce the wear of the FSW tool. The outcome of a double-sided gas metal arc welding (GMAW) was also compared with the FSW process. Furthermore, a systematic investigation into the relationship between the microstructure and toughness of the various subzones of double-sided welded joints was performed.

## 2. Experimental

The 11-mm-thick high-strength X80 pipeline steel plates, whose mechanical property is shown in Table 1, were joined

✉ Corresponding author: Guangming Xie E-mail: xiegm@ral.neu.edu.cn

by GMAW and FSW. The chemical compositions of the pipeline steel and deposited metal are listed in Table 2. The oxide scales were removed from the plate surface before FSW and GMAW, and then the plates were cleaned with alcohol. The GMAW process is shown in Fig. 1(a), and the welding parameters are listed in Table 3. FSW was carried out at a rotation rate of 600 r/min and a traverse speed of 100 mm/min, and preheating at 370°C was performed using four back heating tubes to promote the metal flow and reduce the tool wear, as shown in Fig. 1(b). A W–Re tool (W–25Re, wt%) with a concavity of 20 mm in diameter and a tapered pin of 7 mm in diameter with a thread 6 mm in length was utilized in the FSW.

**Table 1. Mechanical property of X80 pipeline steel**

| Tensile strength / MPa | Yield strength / MPa | Elongation / % | Hardness, HV |
|---|---|---|---|
| 690 ± 5 | 560 ± 6 | 33 ± 0.5 | 220 ± 8 |

**Table 2. Chemical compositions of the pipeline steel and deposited metal** wt%

| Sample | C | Mn | P | S | Si | Ni | Nb | V | Mo | Fe |
|---|---|---|---|---|---|---|---|---|---|---|
| Basal metal | 0.04 | 1.61 | 0.009 | 0.0017 | 0.23 | 0.477 | 0.05 | 0.003 | — | Bal. |
| Deposited metal | 0.04 | 1.25 | 0.013 | 0.012 | 0.35 | 1.55 | — | — | 0.09 | Bal. |

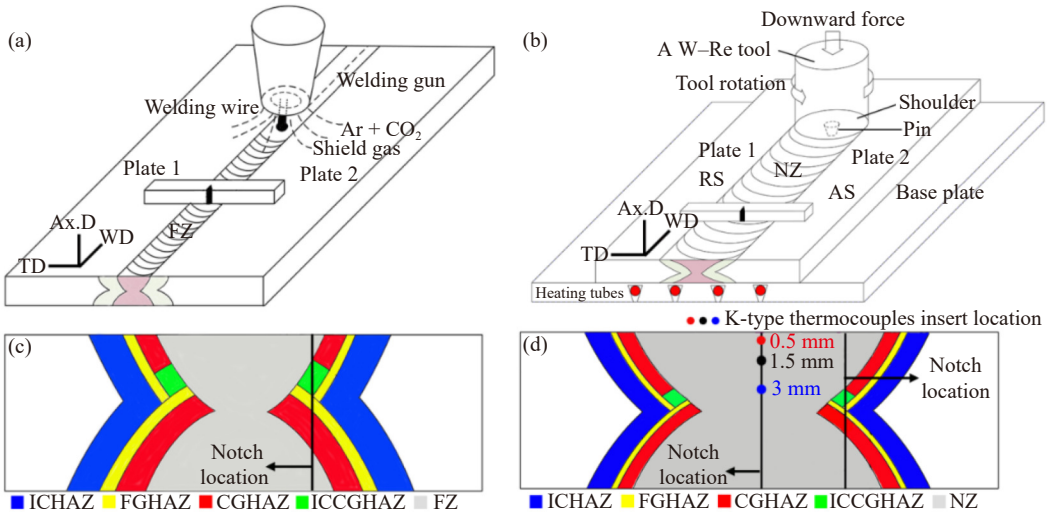


**Fig. 1. Schematic diagrams of gas metal arc welding (GMAW) (a), and friction stir welding (FSW) processes (b), and the V-notch locations for GMAW (c), and FSW impact specimens (d). Retreating side: RS; advancing side: AS; nugget zone: NZ. TD, WD, and Ax.D represent transversal direction, welding direction, and axial direction, respectively.**

**Table 3. Welding parameters for GMAW pipeline steel**

| Welding pass | Wire diameter / mm | Current / A | Voltage / V | Welding speed / (mm·min$^{-1}$) | Shielding gas |
|---|---|---|---|---|---|
| 1 | 1.6 | 300 | 25 | 300 | 82vol% Ar + 18vol% $CO_2$ |
| 2 | 1.6 | 330 | 28 | 270 | |

The thermal cycle histories in the one-pass NZ (NZ1) were measured using a K-type thermocouple and an LR8431-30 acquisition instrument during two-pass FSW. The thermocouples were inserted into a blind hole drilled from the back of the welded plate at depths of 0.5 mm, 1.5 mm, and 3 mm, as shown in Fig. 1(d). The $A_{c1}$ and $A_{c3}$ ($A_{c1}$ and $A_{c3}$ represent start and final austenitic transformation temperatures) phase transformation temperatures of the pipeline steel, measured by a Formastor-II phase transformation instrument, were 672 and 874°C, respectively.

The metallographic samples of the cross-sectional welded joints were prepared perpendicular to the FSW or GMAW directions. The average size of the prior-austenite grains (PAGs) and the maximum width ($W_{max}$) of the M–A constituents were measured using the mean linear intercept method. The microstructure was characterized using a Leica optical microscope (OM), Zeiss Ultra-55 scanning electron microscope (SEM), and FEI Tecnai-F20 transmission electron microscope (TEM). The crystallographic characteristics are obtained using electron backscatter diffraction (EBSD). The samples used for OM and SEM were mechanically polished and etched using a 4vol% natal. The TEM specimens were first mechanically ground to a thickness of 50 μm and then punched into 3 mm diameter disks, and were subsequently electro-polished at −20°C. The samples for EBSD were prepared by electropolishing with an 87.5vol% ethanol solution and 12.5vol% perchloric acid at 25 V for 25 s. The Charpy V-notch impact samples of the weld and HAZ for FSW and GMAW were machined vertically in the welding direction, as shown in Fig. 1 (c) and (d). Specially, the V-notch in impact sample of the

HAZ was through the largest ICCGHAZ to evaluate the weakest average toughness in the whole joint. The impact toughness was tested at an ambient temperature of 20°C. The crack propagation paths through the various subzones were observed, and the schematic diagram of the ductile fracture surface and observation position is shown in Fig. 2.

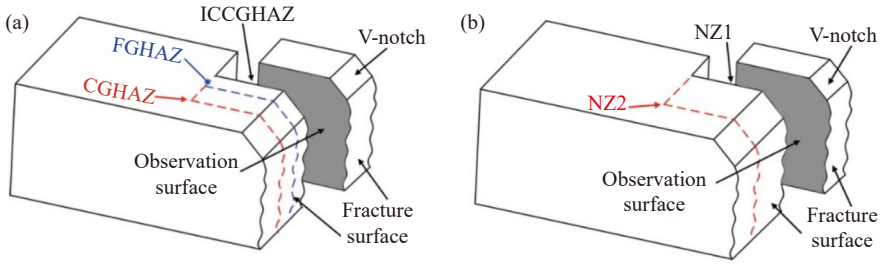


**Fig. 2. Schematic diagram of observed positions for crack propagation paths in the HAZ (a) and NZ (b).**

## 3. Results and discussion

### 3.1. Comparative study on microstructure and toughness in the HAZs of GMAW and FSW joints

Fig. 3 shows the macrographs of the GMAW and FSW joints. Under both wielding processes, defect-free joints were obtained. Based on the microstructural characterization, the GMAW joint consisted of the fusion zone (FZ), HAZ, and basal metal (BM), whereas the FSW joint included the NZ, HAZ, and BM. Based on the variation in the thermal cycle and welding pass, the HAZ consists of four subzones, namely the coarse-grained HAZ (CGHAZ), fine-grained HAZ (FGHAZ), inter-critically HAZ (ICHAZ), and ICCGHAZ. The HAZ of the FSW joint was narrower than that of the GMAW joint, and the ICCGHAZ area of ~1 $mm^2$ for FSW was far smaller than the ICCGHAZ area of ~4 $mm^2$ for GMAW at the low peak temperature and for short duration of the FSW process.

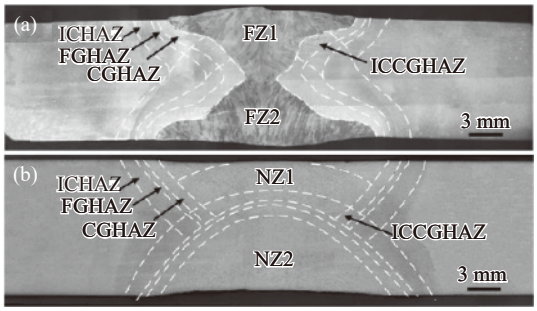


**Fig. 3. Macrographs of the GMAW (a) and FSW joints (b).**

The various subzones in the HAZ of the GMAW joint are characterized by OM, as shown in Fig. 4. As a typical bainitic steel, the BM is composed of acicular ferrite and polygonal ferrite. The ICHAZ consists mainly of polygonal ferrite and fine granular bainite. In contrast, the FGHAZ and CGHAZ contained granular bainite and M–A constituents, and the coarser microstructure located in the CGHAZ. It is known that the peak temperatures in the ICHAZ, FGHAZ, and CGHAZ correspond to various temperatures zones between $A_{c1}$ and $A_{c3}$, slightly higher than $A_{c3}$, and much higher than $A_{c3}$, respectively [18–19]. Therefore, in the ICHAZ of the pipeline steel, at the peak temperature between $A_{c1}$ and $A_{c3}$, a part of the BM was austenitized and then transformed into granular bainite, finally achieving a dual phase of fine GB and ferrite. In the FGHAZ, at a peak temperature just

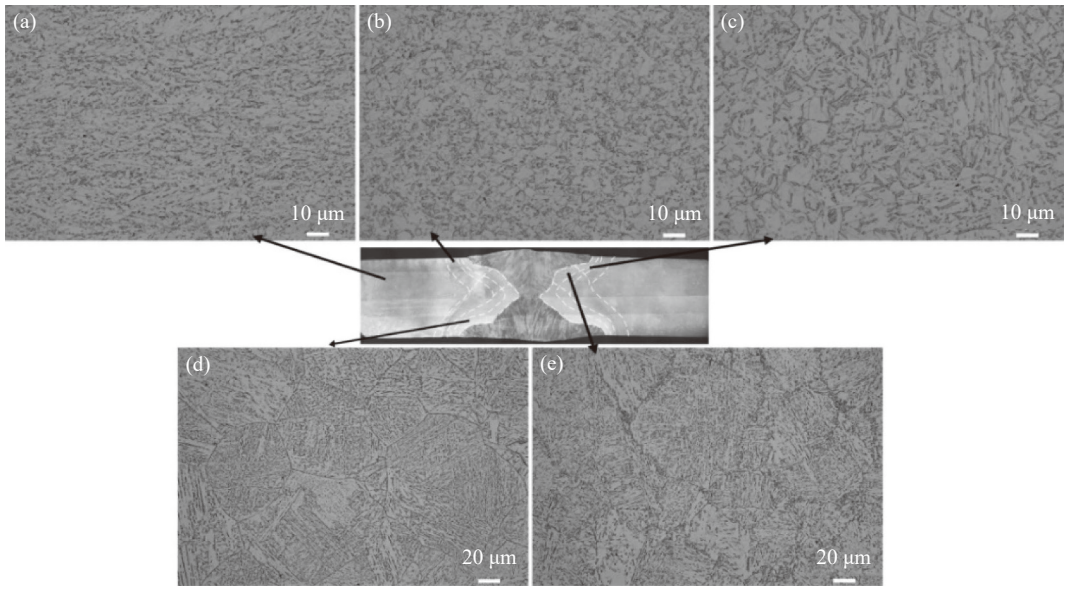


**Fig. 4. OM images of the GMAW joint: (a) BM, (b) ICHAZ, (c) FGHAZ, (d) CGHAZ, and (e) ICCGHAZ.**

higher than $A_{c3}$, the BM was completely austenitized and then transformed into granular bainite. In the CGHAZ, at a peak temperature far higher than $A_{c3}$, the BM was fully austenitized, and then the coarse austenite was transformed into coarse GB. The microstructure in the ICCGHAZ experiencing inter-critical tempering had no noticeable change, and only the partitioning of elements was observed when compared to the CGHAZ. Fig. 5 shows comparative OM images of the FSW joints. Compared to the GMAW joint, the HAZ in the FSW joint also exhibited similar phase constituents. However, the microstructure in the CGHAZ and ICCGHAZ of the FSW joint were relatively fine at the low peak temperature, short duration time, and fast post-weld cooling rate.

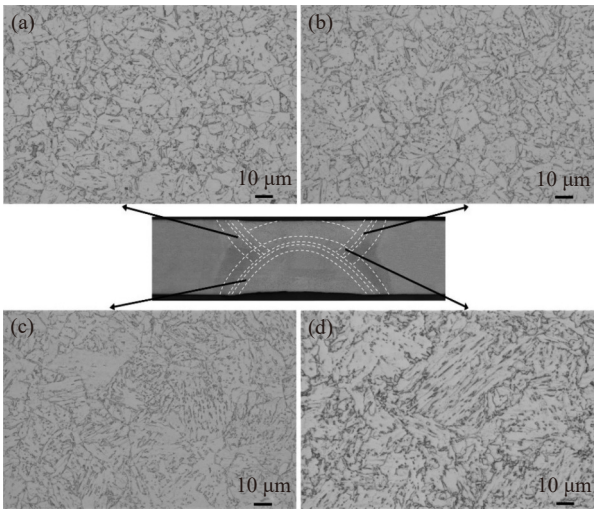


**Fig. 5. OM images of the FSW joint: (a) ICHAZ, (b) FGHAZ, (c) CGHAZ, and (d) ICCGHAZ.**

Figs. 6 and 7 show the SEM and TEM images of the various subzones of the HAZ for GMAW, respectively, depicting the characteristics and distribution of the M–A constituents. In the ICHAZ, FGHAZ, and CGHAZ of the GMAW joint, the island-like M–A constituents were distributed both at the boundaries and within the PAGs, and appeared to be coarsened as they approached the FZ (Fig. 6(a–c)). However, in the ICCGHAZ for GMAW, the M–A constituents were mainly distributed in a network-like structure at the PAG boundaries (Fig. 6(d)). Bainitic ferrite is known to nucleate preferentially at the C-depleted PAG boundaries, and the C-atoms are ejected from ferrite during ferritic growth, thereby forming C-enriched austenite [12,20]. In the ICHAZ and FGHAZ for GMAW, the fine PAGs provided several ferritic nucleation sites. Under low peak temperature and short duration time, the nucleation sites inhibited C-diffusion, leading to a large amount of fine C-enriched austenite being formed. Finally, the C-enriched austenite was transformed into fine M–A constituents during subsequent cooling (Fig. 7(a)). In contrast, coarse PAGs in the CGHAZ resulted in reduced nucleation sites of ferrite, and the combination of a high peak temperature and long duration promoted C-diffusion. Therefore, the C-enriched austenite decomposed into twin martensite (Fig. 7(b)). In the ICCGHAZ, reheated by two-pass welding located in the dual-phase field, C was further partitioned into C-enriched austenite, and the austenite continuously grew and coalesced at the PAG boundaries [21–22]. Thus, coarse network-like M–A constituents distributed along the PAG boundaries were formed in the ICCGHAZ for the GMAW during posting-welding cooling (Fig. 7(c)).

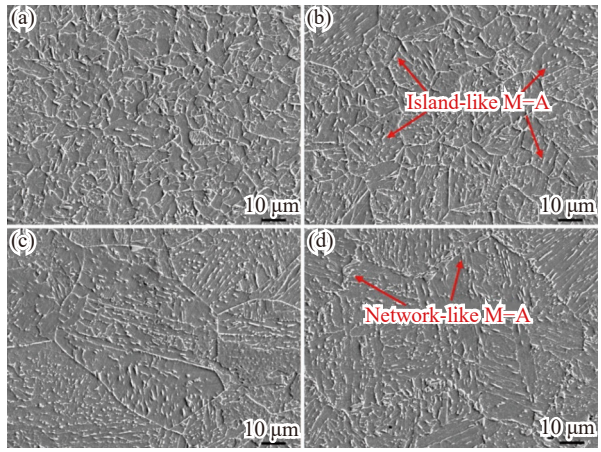


**Fig. 6. SEM images of the GMAW joint: (a) ICHAZ, (b) FGHAZ, (c) CGHAZ, and (d) ICCGHAZ.**

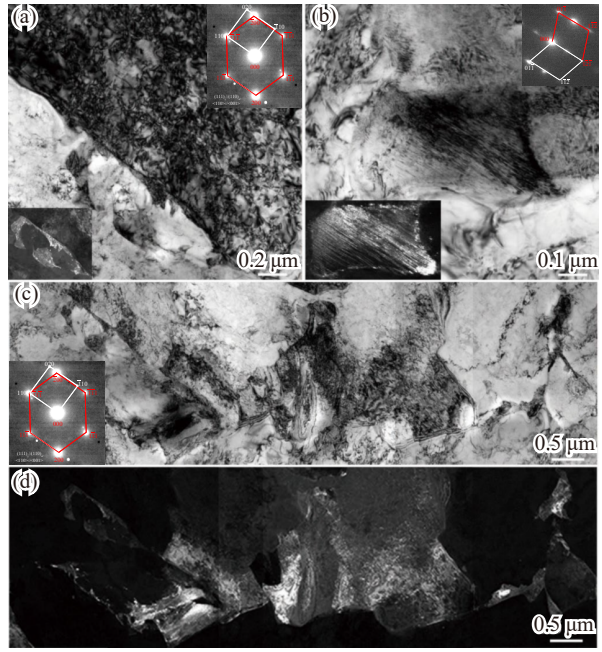


**Fig. 7. TEM images of the fine island-like constituent in the (a) FGHAZ, (b) coarse island-like constituent in the CGHAZ, and (c, d) network-like M–A constituent in the ICCGHAZ.**

Figs. 8 and 9 show the SEM and TEM images of the various subzones of the HAZ for FSW, respectively. Unlike the GMAW joint, the M–A constituents in the ICHAZ, FGHAZ, CGHAZ, and ICCGHAZ for FSW were island-like instead of network-like M–A constituents. As the peak temperature increased, the coarsening of the M–A constituents was not noticeable. Under the low-heat input of FSW, fine PAGs provide more nucleation sites for bainitic ferrite, and C-diffu-

sion is inhibited [12,21]. Therefore, fine island-like M–A constituents were formed in the FGHAZ and CGHAZ, as shown in Fig. 9(a) and (b), respectively. Similarly, in the IC-CGHAZ, the short duration time in the dual-phase field and fast cooling rate during the two-pass welding restrained the formation of network-like M–A constituents (Fig. 9(c)). Furthermore, the retained austenite was mainly distributed at the edge of the M–A constituent in the CGHAZ and ICCGHAZ. This phenomenon can be attributed to the slow C-diffusion and austenitic volume constraint at the α/γ interface, leading to C-enrichment, thereby exhibiting high austenitic stability [4,23].

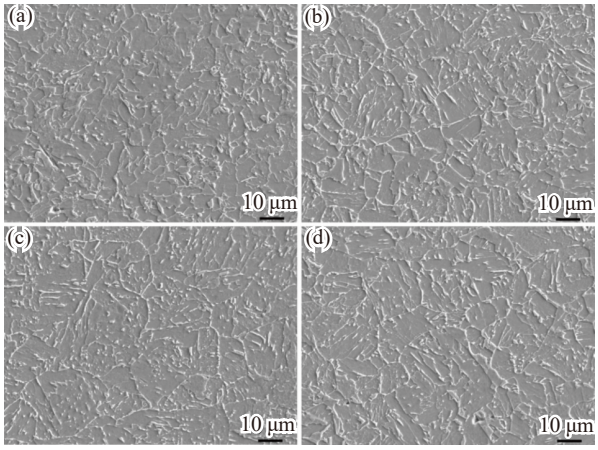


**Fig. 8. SEM images of the FSW joint: (a) ICHAZ, (b) FGHAZ, (c) CGHAZ, and (d) ICCGHAZ.**

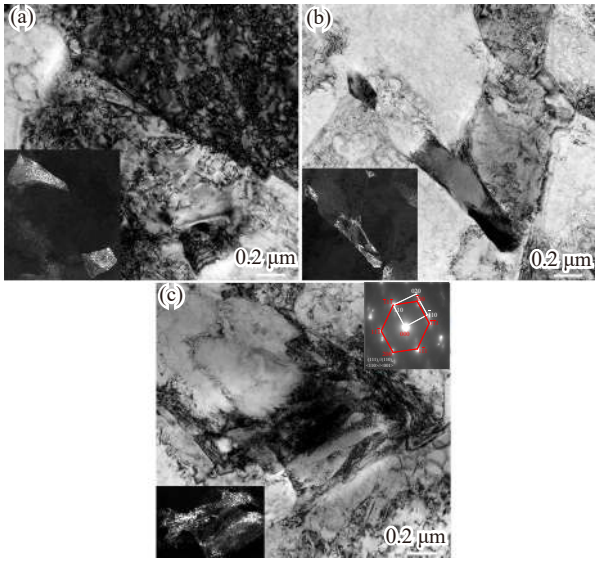


**Fig. 9. TEM images of the FSW joint: (a) FGHAZ, (b) CGHAZ, and (c) ICCGHAZ.**

Fig. 10 schematically summarizes the M–A constituent evolution in the ICCGHAZs for GMAW and FSW. The high heat input during one-pass GMAW led to the formation of coarse PAGs and island-like M–A constituents in the CGHAZ. Subsequently, the CGHAZ was reheated to the dual-phase region between $A_{c1}$ and $A_{c3}$ during two-pass welding, thereby producing coarse network-like M–A constituents in the ICGHAZ owing to the C-partitioning. In comparison, a low-heat input of one-pass FSW resulted in the generation of fine PAG and island-like M–A constituents in the CGHAZ. The short duration time in the dual-phase field during two-pass FSW inhibited the C-partitioning, leading to fine PAG and island-like M–A constituents in the IC-CGHAZ.

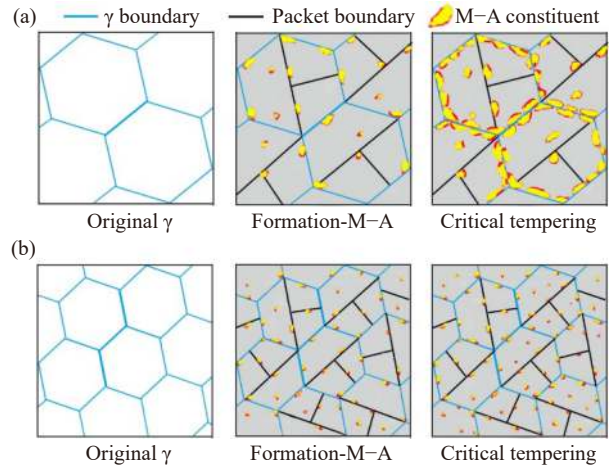


**Fig. 10. Schematic diagram of M–A constituent evolution at the ICCGHAZs of (a) GMAW and (b) FSW joints.**

It is widely accepted that the ICCGHAZ is a zone with the weakest properties in the entire pipeline steel joint; thus, the toughness in the ICCGHAZ was evaluated under current study, as entered in Table 4. The impact energy of the IC-CGHAZ for the GMAW and FSW joints reached 71% and 89% of the BM, respectively, indicating a sound toughness in the ICCGHAZ of the FSW joint. The PAGs and M–A constituents have an important effect on the toughness of the bainitic steel [4,24]. The PAG size and the $W_{max}$ of the M–A constituents in the GMAW and FSW joints are shown in Fig. 11 for reference purpose. The PAGs and M–A constituents were significantly refined in the HAZ of the FSW joint, compared with those in the HAZ of the GMAW joint. It is well known that toughness is an energy concept that included both strength and plastic performances. Energy consumption is needed in the process of crack initiation and propagation, and Eqs. (1) and (2) are used to represent the stress required in the process of crack propagation and initiation [4,25–26].

**Table 4. Impact energy of the ICCGHAZ and NZ for GMAW and FSW** J·cm$^{-2}$

| BM | GMAW-ICCGHAZ | FSW-ICCGHAZ | GMAW-FZ | FSW-NZ |
|---|---|---|---|---|
| 257 ± 8 | 184 ± 5 | 230 ± 6 | 208 ± 5 | 288 ± 7 |

The Eq. (1) below shows fracture strength of metals [4]:

$$\sigma_B = \sqrt{\frac{2}{\pi L}} K_{Ic} \propto \frac{1}{\sqrt{d}} \quad (1)$$

where $\sigma_B$ is the brittle-fractured stress, $K_{Ic}$ is the fracture toughness, $L$ is the characteristic length of brittle failure, and $d$ is the grain size. According to the Eq. (1), the brittle-fractured stress ($\sigma_B$) is primarily influenced by the grain size ($d$).

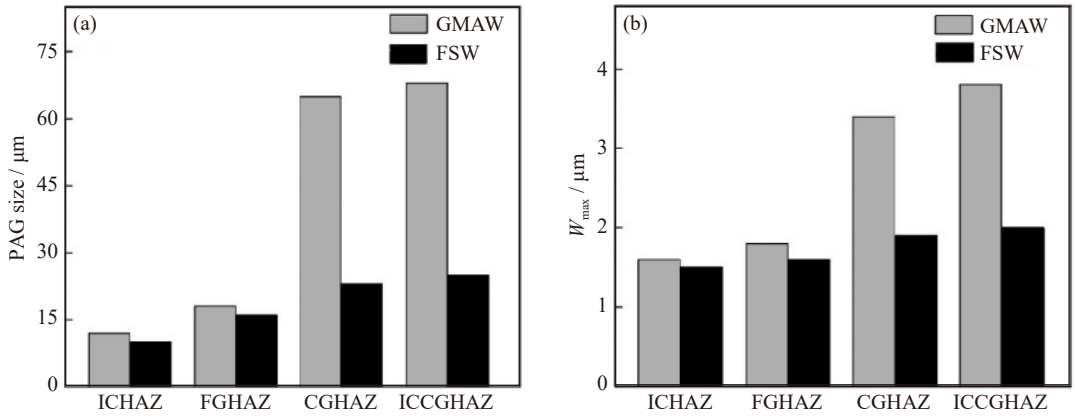


**Fig. 11. Average PAG size (a) and $W_{max}$ of M–A constituent (b) in the GMAW and FSW joints.**

The brittle fracture toughness ($K_{Ic}$) increases with decreasing grain size ($d$), resulting from the high fraction of high-energy grain boundaries, which leads to more energy consumption during crack propagation [27]. Compared with the GMAW joint, the PAGs in the ICCGHAZ were refined, resulting in higher toughness.

The Eq. (2) below gives Griffith-critical stress [25]:

$$\sigma_c = \left(\frac{\pi E \gamma_p}{(1-\nu^2)D}\right)^{1/2} \tag{2}$$

where $\sigma_c$ is the critical cracking stress, $\gamma_p$ is the effective surface energy of the microcrack, $\nu$ is Poisson's ratio, $E$ is Young's modulus, and $D$ is the length of the critical crack. According to Griffith theory, the brittle and hard M–A constituent is considered as a defect, and the microcracks form and propagate at the interface between the M–A constituent and matrix when the stress concentration at the interface exceeds the critical cracking stress [26]. Here, $D$ can be regarded as the $W_{max}$ of the M–A constituent. The $W_{max}$ of the M–A constituent in the ICCGHAZs for GMAW and FSW was 3.8 and 2 μm, respectively, and the $\sigma_c$ was calculated to be 1634 and 2252 MPa. The critical fracture stress decreased obviously with the increase in $W_{max}$; thus, the coarse M–A constituent was another important reason for the significantly decreased toughness in the ICCGHAZ for GMAW.

The ICCGHAZ covered the ICCGHAZ, CGHAZ, and FGHAZ, as shown in Fig. 1. The crack propagated paths in various subzones are shown in Fig. 12. The transformation-induced residual stress and stress concentration between the M–A constituent and matrix can cause cracking when a load is exerted on the joint [20–21]. Furthermore, the PAG size is another important factor affecting toughness, and coarse PAGs promote effective deviation and arrest crack propagation owing to the large number of PAG boundaries. In the GMAW joint, crack initiation was observed near coarse network-like M–A constituents. Also, relatively straight crack propagation paths were observed in the ICCGHAZ (Fig. 12 (a) and (b)). Under the high heat input of GMAW, coarse M–A constituents and PAGs can promote crack initiation and propagation, especially the network-like M–A constituents in the ICCGHAZ can accelerate this process. However, in the ICCGHAZ for FSW, the refined M–A constituents and PAGs can effectively hinder crack initiation and consume more energy during crack propagation, and no network-like M–A constituent was observed. As a result, zigzag paths were formed when the crack encountered the island-like M–A constituents or PAG boundaries (Fig. 12(d) and (e)). The FGHAZs for both GMAW and FSW were composed of

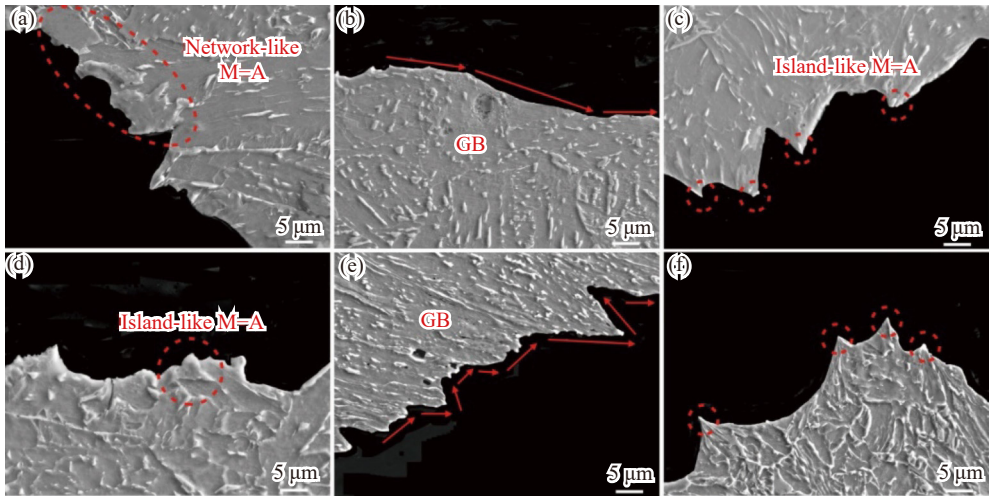


**Fig. 12. SEM images of crack propagation paths in the ICCGHAZ (a, b) and FGHAZ (c) of GMAW joint, and the ICCGHAZ (d, e) and FGHAZ (f) of FSW joint.**

fine M–A constituents and PAGs, which implied a small stress concentration. Therefore, zigzag paths were formed when the crack encountered the grain boundaries during crack propagation, and the toughness was improved significantly (Fig. 12(c) and (f)).

### 3.2. Microstructure and toughness of the double-sided NZs for FSW

Unlike the HAZ, the NZ simultaneously undergoes a thermal cycle and intense deformation during FSW [4,19]. Fig. 13 shows the OM images of the NZ1 and two-pass NZ (NZ2) of the FSW joint. NZ2 contained coarse granular bainite, whereas NZ1 consisted fine ferrite. The M–A constituent morphologies in NZ1 and NZ2 were mainly distributed as island-like constituents at the PAG boundaries and within bainite, indicating similar characteristics. Considering that NZ1 and NZ2 have a set of the same FSW parameters, it was inferred that the difference in microstructure can be due to the reheating effect of the two-pass FSW on NZ1. The NZ contains a higher distortion energy introduced by the FSW, so the reheated temperature can cause static recrystallization of ferrite. In this work, the thermal cycle history of NZ1 during reheating was measured at different locations using thermocouples, as shown in Figs. 1 and 14. The peak temperatures of NZ1 at depths of 0.5, 1.5, and 3 mm from the bottom of the steel plate were 597, 678, and 796°C, respectively, and they increased with increase in measured depth. Recently, it was reported that fine recrystallized ferrite was obtained as warm-rolled low-carbon steel at a reheated temperature of 535°C [28]. Similarly, the stronger deformation of FSW can easily produce ferritic recrystallization when NZ1 is reheated by a two-pass FSW. Furthermore, the preheating exerted before FSW can lead to a lower post-welding cooling rate of longer duration further promoting recrystallization. Therefore, reheating by two-pass FSW and preheating before FSW together caused fine ferrite in the NZ1. Furthermore, when reheating was introduced, M–A constituent was not coarsened. This is attributed to the low density of dislocations and substructures, which reduces the diffusion channels of C owing to recrystallization [29].

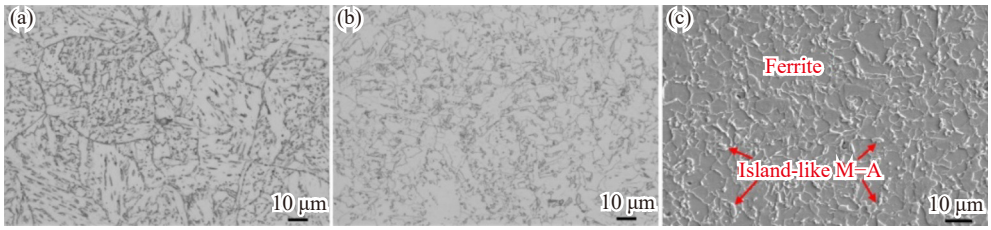


**Fig. 13. OM and SEM images of the NZ2 (a) and NZ1 (b, c) of FSW joint.**

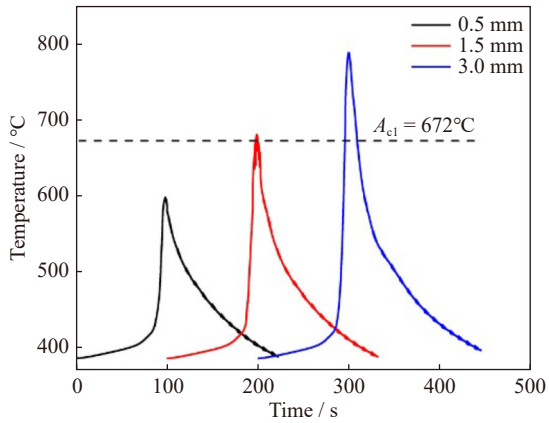


**Fig. 14. FSW thermal cycle histories of NZ1 at different depths.**

Fig. 15 shows the boundary distribution, kernel average misorientation (KAM), and recrystallization distribution maps for NZ1 and NZ2. The low-angle boundaries (LABs) (2° ≤ misorientation angle < 15°) and high-angle boundaries (HABs) (15° ≤ misorientation angle) are represented by yellow and black lines, respectively. The HABs correspond to the boundaries of the PAGs and bainitic packets [30–31]. It was evident that the fraction of HABs in NZ1 was higher than that in NZ2 because of the presence of fine PAGs (Fig. 15(a) and (b)). Similarly, the KAM value in NZ2 was significantly higher than that in NZ1 (Fig. 15(c) and (d)). The recrystallization maps indicated that NZ2 was mainly composed of substructures, whereas NZ1 contained a large number of recrystallized grains (Fig. 15(e) and (f)). Generally, ferrite exhibits high stacking fault energy and high self-diffusivity, and the climbing and cross slip of dislocations are relatively fast, which is favorable for recovery [28,32]. However, recrystallization may occur when the stored energy is sufficient for a strong orientation gradient to appear, as a result of severe deformation [28]. The NZ experienced intense deformation during FSW. During the process, several dislocations and substructures were introduced, leading to high KAM values. However, at the same time many dislocations are also consumed during the recrystallization of ferrite when NZ1 is reheated, resulting in a decreased KAM value.

Fig. 16 shows the TEM images of the NZ1 and NZ2. A high density of dislocations appeared in the NZ2. Considering the microstructure in the NZ2, the original NZ1 obtained under same FSW parameter should have a high stored energy before reheating. Recrystallized ferrite was formed at PAG boundaries and within granular bainite in the reheated NZ1 (Fig. 16(b) and (c)). The growth and coalescence of subgrains and strain-induced boundary migration are two competing mechanisms affecting recrystallized nucleation [28,32]. When the NZ1 was reheated by two-pass FSW, the cross slip and climb of dislocations at elevated temperature promoted the annihilation and rearrangement of dislocations,

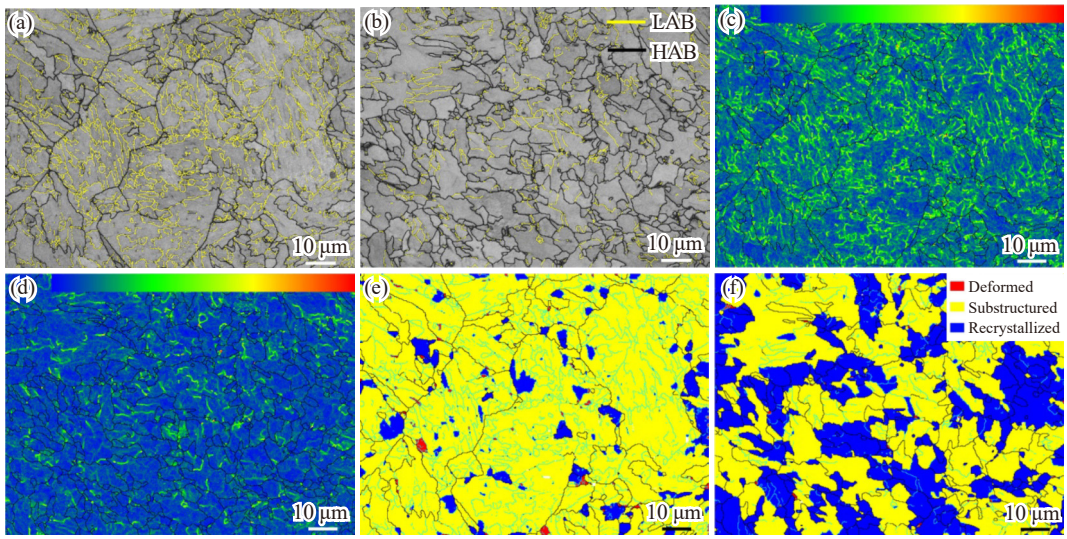


**Fig. 15. Boundary distribution, KAM, and recrystallization maps in the NZ2 (a, c, e), and NZ1 (b, d, f).**

producing a large number of sub-grains. In addition, the observed bulging out of one grain boundary to another indicated that strain-induced boundary migration nucleation occurred during ferritic recrystallization. During the growth of recrystallized grains, the adjacent low-misorientation sub-grains started to rotate, coalesce, and grow. In comparison, the recrystallized grains for strain-induced boundary migration grew through HAB migration [4,32].

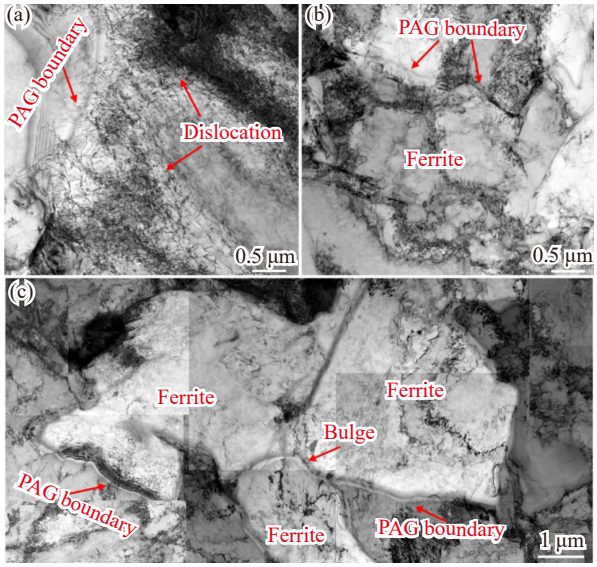


**Fig. 16. TEM images of NZ2 (a) and NZ1 (b, c).**

The impact energy of the NZ reached 112% of that of the BM via impact testing, as shown in Table 4. In comparison, the toughness of the FZ obtained by double-sided GMAW only reached 81% of that of the BM. This is mainly due to the obvious grain refinement in the NZ1. Furthermore, it was observed that the fine grains led to increase in $\sigma_B$ according to Eq. (1), and that more energy is consumed during crack propagation. Fig. 17 shows the crack propagation paths of NZ1 and NZ2. NZ2 consists of fine granular bainite, and that HABs can deflect crack propagation. The PAGs in NZ1 were refined, and the high fraction of HABs and homogeneously distributed M–A constituents led to the difficulty of crack initiation and propagation. Thus, more energy is consumed, and the toughness of the NZ is improved.

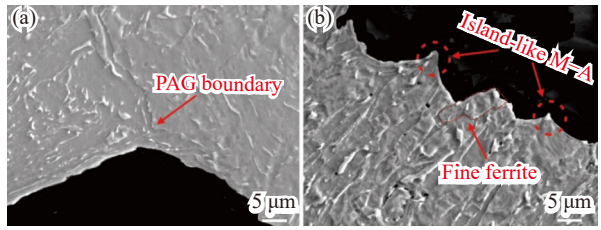


**Fig. 17. SEM images of crack propagation paths of NZ2 (a) and NZ1 (b).**

In the oil and gas transportation field, the deterioration in toughness in the ICCGHAZ of the multi-pass fusion-welded joint significantly influenced the service life and security of thick-wall high-strength pipelines. In this work, the double-sided FSW combined with preheating exhibits a certain advantage in the toughness of the joint, suggesting the viability of FSW for welding method of thick-gauge pipeline steels. We expect that with the gradual development of FSW equipment and tool materials the double-sided FSW will be applied to join the various pipelines in the future.

## 4. Conclusions

In this work, the thick-gauge X80 pipeline steel joint with excellent toughness was achieved by double-sided FSW combined with preheating, and the relationship between microstructure and toughness in the various subzones of the pipeline steel joint was constructed. The detail conclusions are as follows.

(1) Both the CGHAZ and ICCGHAZ of the GMAW joint were composed of coarse GB, and coarse network-like M–A constituents were formed in the ICCGHAZ. However, the GB in the CGHAZ and ICCGHAZ of the FSW joints was refined, and no network-like M–A constituent was generated in the ICCGHAZ.

(2) The toughness of the ICCGHAZ of the FSW joint is superior to that of the ICCGHAZ of the GMAW joint, and it was recorded at 71% and 89% of that of the BM for GMAW and FSW joints, respectively.

(3) In the FSW joints, NZ2 consists of coarse GBs, while NZ1 is composed of fine ferrite. This is attributed to the fact that NZ1 was reheated during the two-pass welding, which led to the static recrystallization of ferrite.

(4) In the entire FSW joint, the toughness of the NZ was highest at 112% of that of the BM. This originates from the fact that the fine grains in the NZ1 can significantly inhibit crack initiation and propagation.

## Acknowledgements

This work was financially supported by the National Nature Science Foundation of China (No. 51774085), Liaoning Province Excellent Youth Foundation (No. 2020-YQ-03), and the Open Research Fund from the State Key Laboratory of Rolling and Automation, Northeastern University (No. 2020RALKFKT009).

## Conflict of Interest

The authors declare no potential conflict of interest.

## References

[1] Y.P. Zeng, P.Y. Zhu, and K. Tong, Effect of microstructure on the low temperature toughness of high strength pipeline steels, *Int. J. Miner. Metall. Mater.*, 22(2015), No. 3, p. 254.

[2] J.B. Ju, W.S. Kim, and J.I. Jang, Variations in DBTT and CTOD within weld heat-affected zone of API X65 pipeline steel, *Mater. Sci. Eng. A*, 546(2012), p. 258.

[3] S.H. Hashemi and D. Mohammadyani, Characterisation of weldment hardness, impact energy and microstructure in API X65 steel, *Int. J. Press. Vessels Pip.*, 98(2012), p. 8.

[4] R.H. Duan, G.M. Xie, P. Xue, *et al*., Microstructural refinement mechanism and its effect on toughness in the nugget zone of high-strength pipeline steel by friction stir welding, *J. Mater. Sci. Technol.*, 93(2021), p. 221.

[5] Z.X. Zhu, L. Kuzmikova, H.J. Li, and F. Barbaro, Effect of inter-critically reheating temperature on microstructure and properties of simulated inter-critically reheated coarse grained heat affected zone in X70 steel, *Mater. Sci. Eng. A*, 605(2014), p. 8.

[6] X.N. Qi, H.S. Di, X.N. Wang, *et al*., Effect of secondary peak temperature on microstructure and toughness in ICCGHAZ of laser-arc hybrid welded X100 pipeline steel joints, *J. Mater. Res. Technol.*, 9(2020), No. 4, p. 7838.

[7] H.J. Aval, Microstructural evolution and mechanical properties of friction stir-welded C71000 copper–nickel alloy and 304 austenitic stainless steel, *Int. J. Miner. Metall. Mater.*, 25(2018), No. 11, p. 1294.

[8] F.C. Liu, Y. Hovanski, M.P. Miles, C.D. Sorensen, and T.W. Nelson, A review of friction stir welding of steels: Tool, material flow, microstructure, and properties, *J. Mater. Sci. Technol.*, 34(2018), No. 1, p. 39.

[9] L.Y. Huang, K.S. Wang, W. Wang, *et al*., Mechanical and corrosion properties of low-carbon steel prepared by friction stir processing, *Int. J. Miner. Metall. Mater.*, 26(2019), No. 2, p. 202.

[10] P. Xue, B.L. Xiao, W.G. Wang, *et al*., Achieving ultrafine dual-phase structure with superior mechanical property in friction stir processed plain low carbon steel, *Mater. Sci. Eng. A*, 575(2013), p. 30.

[11] A. Behjat, M. Shamanian, M. Atapour, and M.A. Sarmadi, Microstructure and corrosion properties of friction stir-welded high-strength low-alloy steel, *Trans. Indian Inst. Met.*, 74(2021), No. 7, p. 1763.

[12] R.H. Duan, G.M. Xie, Z.A. Luo, *et al*., Microstructure, crystallography, and toughness in nugget zone of friction stir welded high-strength pipeline steel, *Mater. Sci. Eng. A*, 791(2020), art. No. 139620.

[13] A. Tribe and T.W. Nelson, Study on the fracture toughness of friction stir welded API X80, *Eng. Fract. Mech.*, 150(2015), p. 58.

[14] Y.F. Sun, H. Fujii, and Y. Morisada, Double-sided friction stir welding of 40 mm thick low carbon steel plates using a pcBN rotating tool, *J. Manuf. Process.*, 50(2020), p. 319.

[15] H. Aydin and T.W. Nelson, Microstructure and mechanical properties of hard zone in friction stir welded X80 pipeline steel relative to different heat input, *Mater. Sci. Eng. A*, 586(2013), p. 313.

[16] J.A. Avila, J. Rodriguez, P.R. Mei, and A.J. Ramirez, Microstructure and fracture toughness of multipass friction stir welded joints of API-5L-X80 steel plates, *Mater. Sci. Eng. A*, 673(2016), p. 257.

[17] J.A. Ávila, C.O.F.T. Ruchert, P.R. Mei, *et al*., Fracture toughness assessment at different temperatures and regions within a friction stirred API 5L X80 steel welded plates, *Eng. Fract. Mech.*, 147(2015), p. 176.

[18] X.D. Li, C.J. Shang, X.P. Ma, *et al*., Structure and crystallography of martensite–austenite constituent in the intercritically reheated coarse-grained heat affected zone of a high strength pipeline steel, *Mater. Charact.*, 138(2018), p. 107.

[19] G.M. Xie, R.H. Duan, P. Xue, *et al*., Microstructure and mechanical properties of X80 pipeline steel joints by friction stir welding under various cooling conditions, *Acta Metall. Sin. Engl. Lett.*, 33(2020), No. 1, p. 88.

[20] X.D. Li, Y.R. Fan, X.P. Ma, S.V. Subramanian, and C.J. Shang, Influence of Martensite–Austenite constituents formed at different intercritical temperatures on toughness, *Mater. Des.*, 67(2015), p. 457.

[21] X.D. Li, X.P. Ma, S.V. Subramanian, C.J. Shang, and R.D.K. Misra, Influence of prior austenite grain size on martensite–austenite constituent and toughness in the heat affected zone of 700 MPa high strength linepipe steel, *Mater. Sci. Eng. A*, 616(2014), p. 141.

[22] X.J. Di, M. Tong, C.N. Li, C. Zhao, and D.P. Wang, Microstructural evolution and its influence on toughness in simulated inter-critical heat affected zone of large thickness bainitic steel, *Mater. Sci. Eng. A*, 743(2019), p. 67.

[23] A. Lambert, A. Lambert, J. Drillet, *et al*., Microstructure of martensite-austenite constituents in heat affected zones of high strength low alloy steel welds in relation to toughness properties, *Sci. Technol. Weld. Joining*, 5(2000), No. 3, p. 168.

[24] G.M. Xie, H.B. Cui, Z.A. Luo, R.D.K. Misra, and G.D. Wang, Asymmetric distribution of microstructure and impact toughness in stir zone during friction stir processed a high strength pipeline steel, *Mater. Sci. Eng. A*, 704(2017), p. 401.

[25] X. Luo, X.H. Chen, T. Wang, S.W. Pan, and Z.D. Wang, Effect of morphologies of martensite–austenite constituents on impact toughness in intercritically reheated coarse-grained heat-affected zone of HSLA steel, *Mater. Sci. Eng. A*, 710(2018), p. 192.

[26] L.Y. Lan, C.L. Qiu, D.W. Zhao, X.H. Gao, and L.X. Du, Microstructural characteristics and toughness of the simulated coarse grained heat affected zone of high strength low carbon bainitic

steel, *Mater. Sci. Eng. A*, 529(2011), p. 192.
[27] J.W. Morris Jr, Stronger, tougher steels, *Science*, 320(2008), No. 5879, p. 1022.
[28] P A. Manohar, M. Ferry, and T. Chandra, Recrystallization of ferrite and austenite, [in] *Reference Module in Materials Science and Materials Engineering*, Elsevier, 2016.
[29] H.B. Cui, G.M. Xie, Z.A. Luo, *et al*., The microstructural evolution and impact toughness of nugget zone in friction stir welded X100 pipeline steel, *J. Alloys Compd.*, 681(2016), p. 426.
[30] H.F. Lan, L.X. du, and R.D.K. Misra, Effect of microstructural constituents on strength-toughness combination in a low carbon bainitic steel, *Mater. Sci. Eng. A*, 611(2014), p. 194.
[31] G.M. Xie, R.H. Duan, Y.Q. Wang, *et al*., Crystallography of the nugget zone of bainitic steel by friction stir welding in various cooling mediums, *Mater. Charact.*, 182(2021), art. No. 111523.
[32] X.Y. Xu, J.Z. Li, W.J. Li, *et al*., Experimental and theoretical study on static recrystallization of a low-density ferritic steel containing 4 mass% aluminum, *Mater. Des.*, 180(2019), art. No. 107924.